HHS Public Access

Author manuscript

Neuroimage. Author manuscript; available in PMC 2018 March 22.

Published in final edited form as:

Neuroimage. 2018 March ; 168: 59–70. doi:10.1016/j.neuroimage.2016.11.033.

Gradient and shim technologies for ultra high field MRI

Simone A. Winkler[a], **Franz Schmitt**[b], **Hermann Landes**[c], **Josh DeBever**[a], **Trevor Wade**[d], **Andrew Alejski**[d], and **Brian K. Rutt**[a]

[a]Department of Radiology, Stanford University, USA

[b]Retired from Siemens AG, Germany

[c]SIMetris Gmbh, Germany

[d]Imaging Research Laboratories, Robarts Research Institute, Canada

Abstract

Ultra High Field (UHF) MRI requires improved gradient and shim performance to fully realize the promised gains (SNR as well as spatial, spectral, diffusion resolution) that higher main magnetic fields offer. Both the more challenging UHF environment by itself, as well as the higher currents used in high performance coils, require a deeper understanding combined with sophisticated engineering modeling and construction, to optimize gradient and shim hardware for safe operation and for highest image quality. This review summarizes the basics of gradient and shim technologies, and outlines a number of UHF-related challenges and solutions. In particular, Lorentz forces, vibroacoustics, eddy currents, and peripheral nerve stimulation are discussed. Several promising UHF-relevant gradient concepts are described, including insertable gradient coils aimed at higher performance neuroimaging.

Keywords

Ultra high field; Gradients; Shims; Magnets; MR hardware technology

1. Introduction

The main motivation for ultra high field (UHF: field strengths of 7 T and above) MRI is the increase in intrinsic signal-to-noise ratio (SNR), allowing for the acquisition of images that have higher spatial resolution and/or higher sensitivity to subtle change than clinical MR images acquired at lower field strengths (3 T and below). These improvements promise to advance our basic understanding of anatomy and physiology in both healthy tissue and disease. As a result, UHF MRI has the potential to become a clinically approved tool for routine monitoring, diagnostics, and treatment planning of both neurological and other disorders with improved sensitivity and specificity.

The scaling of intrinsic SNR with main field strength (B_0) has commonly been described as linear, although recent literature has demonstrated super-linear behavior in the range of 3–

Correspondence to: Brian K. Rutt.

9.4 T (Pohmann et al., 2016). In addition to this SNR benefit, spectral peak separation for NMR applications increases linearly with B_0. Structures and lesions that are hidden in the noise floor at lower fields may become detectable at UHF, and peaks in the NMR spectrum that overlap at lower fields may be separately detected at UHF.

Recently, and especially through the worldwide interest in the NIH Human Connectome Project (HCP) (Van Essen et al., 2012, 2013; Ugurbil et al., 2013; Vu et al., 2015; Hodge et al., 2016; Tomasi et al., 2016), it has become quite clear that new high resolution structural, functional, and diffusion imaging methods are capable of providing insights into human brain structure and function that were not considered possible even a few years ago. The increased SNR at UHF can be used to resolve structural changes at the sub-400 μm level, functional/connectivity networks at the sub-millimeter level, and tissue microstructural patterns at the sub-20 μm level (by advanced diffusion methods). However, we now know that there is a "hidden requirement" if we are to extract the full intrinsic SNR benefit of UHF and therefore to achieve the promised spatial, spectral, and diffusion resolution rewards: we will require order-of-magnitude performance improvements in the gradient and shim systems over the hardware that is currently built into even the newest clinical systems (Cohen-Adad et al., 2012; Kimmlingen et al., 2012; McNab et al., 2012; Setsompop et al., 2012; Tisdall and Wald, 2012; Wedeen et al., 2012). To achieve the higher resolutions made possible by the higher intrinsic SNR at UHF, larger gradient areas are required (noting that it is the *maximum area* under a gradient encoding pulse that determines the highest achievable spatial resolution). This can be achieved using existing gradient technologies by lengthening gradient encoding pulses without increasing their amplitudes; unfortunately, this approach leads to a loss of SNR especially at UHF as a result of T2-related signal decay during the increased encoding time, compounded by shorter T2 relaxation times at UHF. Therefore, achieving the full SNR benefit of UHF requires gradients that are stronger and can be switched faster than present-day gradient systems, so that larger gradient encoding areas can be achieved *without* the use of longer gradient pulses, and in fact ideally using shorter encoding pulses. In order to implement this increased performance, it will be necessary to increase gradient currents and voltages and possibly even to redesign both gradient and shim systems.

The gradient system produces one of three magnetic fields that are necessary to make MRI work – the linearly varying (in space) z-component of magnetic field B_z, which is responsible for spatial encoding, diffusion encoding, and other aspects of the imaging process. Note that the other two components of the magnetic field, B_x and B_y, do not contribute to spatial or diffusion encoding, but do contribute to side effects such as induction of eddy currents in nearby conductive structures, and peripheral nerve stimulation in the human subject –these two side effects are discussed in greater detail below. While the other two types of fields (the static magnetic field B_0 and the radio frequency (RF) field) depend on each other, the gradient fields are independent of B_0, and as such the same set of gradient coils and gradient power supplies (drivers) can in principle be used at any static field strength. This means that the basic design principles for gradients intended for use at UHF are the same as for standard (lower field) MRI. However, despite this general principle, we now understand that it is necessary to push gradient performance considerably higher at UHF, as outlined above. Because of the increased demands on performance, it is important

to understand and re-evaluate the limits of gradient and shim performance. In addition, it is clear that for safe and reliable operation, gradient and shim systems must be adapted to the challenging UHF working environment. In particular, electro-magneto-mechanical interactions are of concern when increasing the main field strength to UHF levels.

In this review, we provide 1) an overview of MR gradient and shim systems and the factors that determine gradient and shim performance; 2) the engineering challenges that are a direct consequence of operating these high-performance coils at UHF, particularly in terms of patient safety; 3) the effect of the increased static magnetic field strength on image accuracy/quality; 4) an overview of dedicated gradient concepts suitable for UHF; and 5) other additional noteworthy topics in UHF MRI that are related to space- and time-varying magnetic field gradients.

2. UHF gradient system components

The gradient system is divided into several subsystems: the gradient coil (GC), the gradient driver or power amplifier (GPA), and the interconnecting parts such as cables, filters, connectors, etc. Also considered a part of the gradient system are shim coils and passive shims when they are built into the GC. We describe these basic components of the overall gradient system in the paragraphs below and make special mention of any adaptations that are considered important towards safe operation or optimized performance when used within the more challenging UHF environment.

2.1. Gradient coil

UHF MRI systems designed for human use are always implemented using horizontal-bore cylindrical superconducting magnets. In such a configuration the gradient coil is usually cylindrical and is centered in the magnet bore. The epoxy-potted thick-walled cylinder of an actively shielded GC (Fig. 1 left) embeds several parts of the GC including its main components: the three separate gradient coil windings representing the X- and Y-gradients (Fig. 1 right) and the Z-gradient (Fig. 1 center). Each GC winding consists of an inner primary layer and an outer shield layer, the latter acting as a shield to reduce the stray field of the GC within the magnet cryostat and the resulting eddy currents and secondary magnetic field distortions which lead to image artefact (Pillsbury and Punchard, 1985; Turner, 1986, 1988, 1993; Crozier et al., 1994; Chapman, 2006).

The winding patterns of the X- and the Y-gradients are very similar, but rotated 90° with respect to each other, and typically follow a pattern such as shown in Fig. 1 right. The term “transverse” gradient is often used to describe the common characteristics that X- and Y-gradients share. A standard Z-gradient consists of a set of circular wires (hoops) arranged in parallel on a cylindrical shell (Fig. 1 center), with current flowing in opposite directions between front and back sets of hoops.

The main function of a gradient coil is to spatially modulate the main magnetic field in a predictable way, thereby causing the Larmor frequency of spins to vary as a function of position. This allows spatial encoding of the MR signal. This is achieved by producing a controllable time-varying magnetic field (typical gradient waveforms contain frequencies in

the 0–3 kHz range), which is achieved by driving currents through the winding patterns shown in Fig. 1 center and right. Electrically, the main characteristics of the gradient coil windings are therefore resistance (typically < 150 mΩ at DC) and inductance (typically < 1000 μH). It is important to note, however, that this intended functionality comes at the cost of a number of system complexities that need to be carefully managed in order to yield a safe and optimized GC design. These complexities include not only electromagnetic, but also cooling-related flow, thermal, vibration, acoustic, and other physical characteristics. A properly designed GC needs to meet strict performance specifications within each of these categories in addition to the more fundamental gradient efficiency and homogeneity requirements that primarily govern image quality, while at the same time operating within safe limits to protect the coil itself as well as the subject in the scanner and the operator.

2.2. Gradient power amplifier (GPA)

Modern GPAs most commonly use Pulse Width Modulation (PWM) amplifiers as they provide high power at low loss and high fidelity (Mueller et al., 1991; Ideler et al., 1992; Mueller et al., 1993). The principle of operation is that a train of very short (sub-μs length) voltage bursts (several hundred volts amplitude) is applied. The on/off ratio of these bursts is varied in order to provide the needed total voltage and current to the GC. High performance amplifiers incorporate a cascade of several such PWM amplifying modules. This type of architecture allows for very high output voltages (up to 2500 V) and currents (up to 900 A).

Gradient amplifiers are class-D PWM-based linear current amplifiers which must be tuned to the impedance of the attached gradient coil using feed-back and feed-forward parameters to match fidelity targets. Important specifications (with typical modern-day values in brackets) are peak voltage (> 1500 V), peak current (> 500 A), bandwidth (> 10 kHz), gain accuracy and linearity (< 0.05%), and high output fidelity (total harmonic distortion < 0.25%).

One minor drawback of PWM amplifiers is output noise caused by the rapid switching, which is greatly reduced by the use of advanced filtering methods. Filtering reduces gradient current ripples without restricting the spectral characteristics needed for proper pulse sequence generation. The gradient system typically incorporates electrical filters, some of which are mounted at the penetration wall between magnet room and equipment room. These filters remove unwanted noise and high frequency interference from the gradient current waveforms, while maintaining the integrity of the RF shielding intended to prevent leakage of RF signals into and out of the shielded room. These filters are typically realized as lowpass or bandstop filters. Fig. 2 shows the GPA and its connection to the GC, which is illustrated using the resistance and self-inductance of the coil for simplification purposes.

2.3. Shim coils

Other components that are physically attached to the GC will be mentioned in this review as they interact with the GC. Among these, passive and active shims play a key role in the GC system design process, and in the resulting MR image quality.

2.3.1. Correction of magnet inhomogeneities via shimming—One of the greatest challenges in UHF MRI is achieving an extremely homogeneous static magnetic field – on the order of ± 1 μT or better across the entire imaging volume – in order to avoid unnecessary signal loss and geometric distortion. Both superconductive and passive shims are used to correct the inhomogeneities that result from magnet manufacturing tolerances and site influences (Chen and Hoult, 2005; Koch et al., 2009), and are not usually adjusted after the initial commissioning of the MRI system. Typically, UHF magnets have superconductive shims implemented, which is often not the case for clinical magnets at 3 T and below. The superconductive shims are located inside the main superconductive magnet and are designed and built as part of the main magnet. Passive shimming involves the strategic placement of passive iron pieces around the imaging volume. Sometimes these shim iron pieces are positioned inside slots of the GC, depicted on the front face of the GC in Fig. 1 right. Magnet homogeneity following superconductive and passive shimming can be as low as 1 ppm (< 10 μT for UHF magnets) over the imaging region.

2.3.2. Shimming of patient-specific field inhomogeneities—Compensation for patient-induced B_0 field inhomogeneities requires sophisticated hardware and software, used together to accomplish what is known as “patient-specific B_0 shimming” (Gruetter and Boesch, 1992; Gruetter, 1993; Shen et al., 1999; Hetherington et al., 2006; Koch et al., 2009). UHF MRI systems need to have improved patient-specific shimming capability compared to lower field systems. As the main field strength increases to 3 T and beyond, the patient's body itself becomes the primary cause of B_0 distortions. These patient-induced field inhomogeneities are mostly generated at interfaces of different tissue types (exhibiting diamagnetic characteristics) with air (exhibiting paramagnetism), and these inhomogeneities increase at UHF. Patient-induced B_0 variations can easily exceed 10 μT near the air-filled cavities of the ears, nose and mouth.

Conventionally, spherical harmonic decomposition is used to describe the amount and type of field distortion that is caused by B_0 inhomogeneity. The B_0 field variation is decomposed into spatial field variations of 0th (uniform), 1st, 2nd, 3rd (and higher) degree spherical harmonics. In lower field systems, we observe significant distortions up to the 2nd degree, while for UHF systems these field variations can require correction up to 3rd and even higher degrees (Spielman et al., 1998; Pan et al., 2012). High quality higher order/degree shimming is therefore essential, not only in basic structural imaging, but particularly in more B_0-sensitive functional, quantitative, and spectroscopic imaging methods that rely on higher field homogeneity for achieving extremely stable measurements and fine spectral resolution.

In practice, this capability of basic B_0 shimming is achieved through the use of independent room-temperature (non-superconductive) resistive shim coils, each driven by an individual shim power supply. A standard resistive shim embodiment consists of a set of coils, each one producing an independent spatial field distribution within the imaging volume. Most commonly, each of these spatial field distributions approximates a certain spherical harmonic (SH).

0th degree shimming (to correct for uniform field offsets) can be accomplished either by using a shim coil that produces a uniform field or by dynamically adjusting the center

frequency of the receiver. 1st degree resistive shimming is usually accomplished by the GCs themselves (e.g. by adding DC current offsets to each of the three gradient axes). Higher degree field compensation requires a set of the aforementioned independent higher degree shim coils, typically one single-wired layer per spherical harmonic term. Sometimes these coils become part of a physically separate MR hardware component, but most commonly they are incorporated into the GC structure, making efficient use of the available space between primary and shield gradient windings. Human UHF MRI systems commonly implement 2nd and sometimes 3rd degree SH shims, whereas 4th, 5th and even higher degrees have been studied occasionally but are much less commonly found on present-day scanners (Spielman et al., 1998; Pan et al., 2012). At 7 T, typical 2nd degree shimming restores field homogeneity to approximately 0.7 μT (30 Hz) over the entire brain, with peak B_0 errors of approximately 2.5 μT (100 Hz) still present near the air-filled cavities of the ears, nose and mouth (Pan et al., 2012). The addition of 3rd degree shims reduces these worst-case B_0 errors by about a factor of two, to approximately 1.25 μT (50 Hz) (Pan et al., 2012).

2.3.3. Multi-coil shim arrays—As mentioned above, local patient-induced field inhomogeneities often exhibit high spatial orders of change. A growing body of work shows that at UHF, the most commonly implemented higher order resistive shims (up to 2nd degree) are not enough to counteract these patient-induced field inhomogeneities (Pan et al., 2012).

A recently introduced alternative to resistive SH shimming is the use of resistive multi-coil (MC) shim arrays (Juchem et al., 2011; Juchem et al., 2013). These MC shim arrays do not model and correct the field using spherical harmonic basis functions and the corresponding shim coil geometries, but rather consist of an array placed in close proximity to the subject and formed from a large number (32–128) of identical small loops (typically 5–10 cm in diameter), each loop driven independently at relatively low current. The large number of small loops in these arrays, and the close coupling to the body that has been most typical of these “local” MC arrays, offers high flexibility and the ability to generate sophisticated higher order compensation for B_0 inhomogeneities, which can improve on the correction provided by conventional spherical harmonic shims.

The reduced size and current requirements of MC shim arrays offer the possibility for rapid adjustment of loop currents and therefore the opportunity for dynamic shim adjustments, in which B_0 inhomogeneities are compensated in real time. Dynamic shimming is also possible with more conventional spherical harmonic shims, albeit at slower switching rates compared to MC shim arrays. Dynamic shim adjustment has a number of applications, e.g. the optimization of field homogeneity over each individual slice of a multi-slice 2D MR scan for applications that demand particularly homogeneous B_0 fields, such as echo planar imaging (EPI) and multi-voxel spectroscopy. Additional advantages of MC shim arrays are their intrinsic similarity to receive and transmit RF coil arrays. As a natural extension of this latter concept, a merging both of RF and shim functions into a single device has recently been proposed by several groups (Han et al., 2013; Truong et al., 2014; Stockmann et al., 2016). The great advantage of such a combined device is the prospect for extremely efficient packaging of this hardware into a single closely coupled (tight fitting) coil array. In

principle, this maximizes efficiency and capability of both RF and B_0 shimming systems, with minimal reduction in the performance of either system (Stockmann et al., 2013; Winkler et al., 2015).

2.3.4. Electromagnetic interactions between shim and gradient coils—Ideal gradient systems are electromagnetically isolated from their environment as shown in Fig. 2. However, in reality, coupling exists between gradients and shims and even between gradients and the main magnet via inductive, capacitive and mechanical (Lorentz) interactions. At UHF, these coupling phenomena become prominent and need to be dealt with. Fig. 3 shows an extension of the simple GC model in Fig. 2, with added shim coils and a shim power supply. Capacitor symbols have been added to Fig. 2 to indicate potential coupling. In particular, the coupling between gradient and shim coils is relevant. The use of resistive shim coils of 3rd or even higher degree spherical harmonics adds a new challenge to the design of the gradient system. Some of these higher degree shim coils can strongly couple with a gradient coil. When coupling occurs, pulsing the gradient will lead to high levels of induced currents flowing in the affected shim coil. Special effort needs to be made to decouple these higher order shims at the shim / GC design stage, as otherwise gradient pulsing will perturb the higher order shim functionality and may even damage the shim power supply.

3. UHF-specific gradient technology challenges: safety

To a first approximation, the design and implementation of the gradient system is not affected by the choice of main magnetic field. However, at UHF some of the secondary effects originating in the gradients can have serious consequences and can be detrimental and even dangerous. These challenges include but are not limited to: 1) larger Lorentz forces, leading to higher levels of vibration and acoustic sound generation, and 2) peripheral nerve stimulation (PNS). In addition, the higher current densities employed in gradients at UHF to achieve higher performance exacerbate these issues significantly. These challenges are addressed below.

3.1. Lorentz forces

One of the greatest engineering challenges for UHF gradient technology is mechanical: the conductors of MR GCs are subject to large Lorentz forces due to rapidly switched currents in the presence of the ultra high static magnetic field. These Lorentz forces cause GC conductor vibrations, which generate displacement of the GC surfaces and in turn the patient bore wall and other surfaces and structures of the MR scanner. This leads to vibrations that can induce motion artefact in images, as well as the generation of acoustic sound pressure levels (SPLs) that are well above 100 dB. In more extreme cases, gradient conductor displacements could theoretically lead to loosening of components and even damage to the GC and the MR system as a whole; therefore, understanding and reducing Lorentz forces becomes critical at UHF.

Alternating currents create oscillatory Lorentz forces when a static magnetic field is present. The Lorentz force vector $d\mathbf{F}$ that acts on a small GC conductor segment of length dl is described by the cross product of the main magnetic field vector $\mathbf{B_0}$ and the current vector $\mathbf{I}$.

$$d\mathbf{F} = dl \cdot (\mathbf{B_0} \times \mathbf{I}) \quad (1)$$

Eq. (1) tells us that when current is flowing in a conductor segment that is oriented in any direction except for parallel to the main magnetic field lines, non-zero Lorentz forces perpendicular to both $\mathbf{B_0}$ and the conductor direction will be generated (Mansfield and Chapman, 1986).

At conventional static magnetic field strengths of 1.5 T and 3 T, Lorentz forces and the vibrations and acoustic noise that result, are already a significant concern with regard to patient comfort and safety. At UHF, these concerns can become extreme if not properly managed. Some of these challenges and their proposed mitigation are outlined in detail below.

3.2. Vibrations

3.2.1. Vibrations in the magnet-gradient assembly—Time-varying currents flowing in the gradient conductors produce time-varying Lorentz forces according to Eq. (1), that cause vibrations of the conductor and in turn the whole mechanical assembly of the GC. As both the peak current / current density in the GC and the static magnetic field strength increase, these forces will become extreme. Peak currents as high as I_{max} = 900 A are applied to the GCs in modern-day MRI systems. With over 200 m of wire for each gradient winding running inside the GC, this means that an impressive amount of force needs to be managed at UHF. According to Eq. (1), the worst-case force at 11.7 T could approach 2×10^6 N (equivalent to a weight of 200 metric tons), if the entire length of the conductor were oriented in a direction perpendicular to B_0. This is more than an order of magnitude higher than the worst-case force of approximately 90 kN at 1.5 T for the lower currents (e.g. 300 A) typically used in existing clinical scanners. In addition to Lorentz forces, the GC may also exhibit a net torque, which similarly increases with field strength.

Fortunately, these Lorentz forces and torques are largely balanced inside the GC, such that the net force is only a small fraction of the above worst-case scenarios, explaining why the net movement or vibration of the GC has been manageable to date, even for UHF magnets. To achieve complete Lorentz force and torque balancing, the GC conductor geometry needs to be designed with care, employing knowledge of the spatial distribution of the main magnetic field, in order to cancel all net forces and torques acting on the GC as a whole.

As the main magnetic field strength increases into the UHF range, and as GC currents increase with the availability of newer gradient driver and coil technologies, and finally as magnets become smaller, shorter, and more tightly shielded, these net Lorentz forces and torques will increase, leading to significant future concerns related to vibrations and acoustic noise.

3.2.2. Mechanical resonances—The vibrations of the cylindrical GC shell will be significantly increased at specific mechanical resonances that correspond to the eigenmodes of the cylindrical gradient shell. This can result in motion-related image artefacts, but can

also lead to very high local strains and mechanical GC damage or even a superconductive magnet quench. Such mechanical resonances are excited when both (a) the GC wire vibrations couple to one particular eigenmode of the cylindrical gradient shell, and (b) when in addition that wire layer is driven with currents matching the resonance frequency of that eigenmode. Typical MRI pulse sequences use gradient waveforms containing frequencies in the range of 0–3 kHz; unfortunately many of the mechanical resonances lie in this same frequency band. In order to reduce the likelihood of exciting mechanical resonances during imaging, these resonant frequencies can be specifically avoided (or filtered out) in the pulse sequence (this is not always possible, but can be achieved in part for EPI sequences that use pure sinewaves for the EPI readout gradient) (Oesterle et al., 2001; Tomasi and Ernst, 2003).

More fundamentally, it may be possible to shift the eigenmodes of the cylindrical shell to higher frequencies by reducing overall dimensions of the GC, by increasing its wall thickness, or by adding mass and/or or stiffness. This strategy, for example implemented in reduced-dimension head gradients that will be described below, may be a viable way to increase eigenmode frequencies up to the top end of the pulse sequence frequency band, thereby reducing the detrimental effect of these mechanical resonances.

3.2.3. Low frequency vibrations—Low frequency movements (i.e. shaking) are restricted to frequencies below 100 Hz and have not been a major problem for UHF systems to date. This is due to the fact that most existing UHF magnets are extremely long and not actively shielded; such magnet designs are characterized by a very homogeneous magnetic field, not only in the area of the field of view, but extending over the entire GC. Each individual GC winding forms a closed loop beginning and ending approximately at the same location. This means that every small amount of current producing a local Lorentz force will be counteracted at another location on that same loop. Hence in a homogeneous field no net force will exist. Due to relatively stiff construction, the GC cylinder primarily undergoes bulk displacements (i.e. no bending or flexing) in the low frequency range. Since such steady state movements can only be excited by net forces, there will not be much movement in the low frequency range for these longer magnets.

This situation is different with shorter magnets with actively reduced fringe field, as in these magnets the field homogeneity the region encompassing the GC is affected. For this reason, higher net forces and therefore stronger low-frequency vibrations are expected with shorter UHF magnets. As UHF systems progress toward clinical translation, magnets will be redesigned to be lighter, smaller, and shorter, and this force-balancing and low-frequency vibration issue will become more important. One solution commonly employed in industrial practice is to redesign the GC with knowledge of the inhomogeneous field it will be placed in, to ensure that it is force- and torque-balanced.

3.2.4. High frequency vibrations—As described above, high local Lorentz force amplitudes are produced along the wires of the gradient windings when driven at high current. At frequencies above 100 Hz, the GC cylinder starts to vibrate and deform mechanically, following the shapes of its natural mechanical resonances or eigenmodes. These resonant modes can cause bending, breathing, ovaling, and torsional deformation of the GC cylinder shell. One example of a bending deformation is the so-called “banana”

vibration mode shown in Fig. 4 left, which often dominates GC vibration. On the other hand, in breathing deformations the GC the shell diameter expands and contracts (Fig. 4 right). The greatest concern is that when driven at these mechanical resonances, even small gradient currents can cause high vibration amplitudes. At frequencies that fall in between resonances, the GC vibrates according to a mix of deformation shapes, and with significantly reduced amplitude of surface deflection compared to the resonant situation.

At UHF, the surface deflections caused by these vibrational modes increase in amplitude, as the Lorentz forces that cause coil deformation are much larger. Maximum vibration amplitudes of GCs at UHF reach the range of 100–200 μm within the 0–3 kHz window generally used for MR imaging pulse sequences. This increases the risk of image artefact, and can even lead to coil damage. Compared to their use at standard lower-field MRI systems, GCs operating at UHF thus need to manage a much larger amount of vibrational energy. Considering the 700 kg mass of a typical GC cylinder, it becomes obvious that very strong internal bonds are necessary to prevent the GC cylinder from breaking apart. The use of an epoxy resin material with a superior stiffness matrix and special vacuum potting techniques to avoid delamination and other internal failure modes are essential.

3.2.5. Accurate analysis of high-frequency vibrations—As a result of the concern about GC vibrations at UHF, several groups have developed tools for accurate analysis by means of numerical simulation. Progress in this area has been facilitated by ever-advancing computing performance. Multiphysics modeling has gained significant importance in MRI over the last few years and is now commonly applied to vibrational analysis, opening up significant new insights (Zorumski, 1973; Edelstein et al., 2002; Mechefske et al., 2002; Mechefske et al., 2004; Shao and Mechefske, 2005; Taracila et al., 2005; Mechefske and Wang, 2006; Koch et al., 2009; Winkler et al., 2014; Winkler et al., 2015). State-of-the-art multiphysics overmodeling methods demonstrate a high level of agreement with experimental results (Lerch et al., 2000; Mechefske et al., 2002; Mechefske et al., 2004; Yao et al., 2004; Rausch et al., 2005; Mechefske and Wang, 2006; Liu et al., 2011; Jiang and Havens, 2012; Goora et al., 2013; Liu et al., 2013; Winkler et al., 2014; Wang et al., 2015; Winkler et al., 2015). Experimentally validated modeling can then be used to gain new understanding into the causes and types of vibrations observed in GCs. Such simulations have been used to study lower-field systems, and more recently have been applied to the study of GCs operating at UHF.

These new modeling tools should be valuable at the design stage for future-generation GCs. As computational capability increases, we can anticipate the ability to build models that include not only the GC and its immediate surroundings as is currently done, but to include more of the extended scanning environment including the magnet (with all internal details of the cryostat), cables, room walls, and more. It has been shown experimentally that vibrational pathways between various components of the MR system, as well as vibrations of structures other than the GC itself, can play a key role in the overall vibrational and acoustic footprint of a system (Edelstein et al., 2002). This is particularly applicable to UHF with its larger overall system size and component complexity; a fully featured multiphysics model will accelerate the progress toward vibration-reduced UHF GCs.

3.2.6. Lorentz damping—One novel insight confirmed by the new modeling capabilities described above that proves particularly noteworthy for UHF applications, is the existence and analysis of a newly observed phenomenon called Lorentz damping (Winkler et al., 2015). By this theory, the intrinsically stronger vibrations of GC conductors exposed to higher field strengths lead to greater mechanical damping compared to lower fields.

Newly established modeling tools form the ideal platform to study this new effect. Using these tools, we are only now beginning to understand the significance of the Lorentz damping effect in relation to GCs operated at UHF, but it is already clear that conventional assumptions about the linear scaling of vibrations and acoustics according to Eq. (1) may be incomplete. Instead we now understand that there may be a nonlinear dependence on field strength (Moelker et al., 2003), leading to lower levels of vibration and acoustics than anticipated. This should alleviate some concerns and improve the prospects for clinical translation of UHF MR systems.

3.2.7. Reduction of high-frequency vibrations—There is likely no viable means to eliminate all of the mechanical resonances occurring in GC operation, however, the resonant peaks can be shifted and/or attenuated to some extent by careful choice of GC construction materials and/or gradient size. For example, technical ceramics have a higher modulus of elasticity than epoxy resins, and their inclusion (perhaps in the form of an inner gradient bore liner (Winkler et al., 2016)) would therefore be expected to shift the peaks to higher frequencies. Having said this, it is likely not practical to build a GC entirely from ceramic material due to concerns about mechanical brittleness. Additional efforts in literature have also suggested the positioning of the GC within a vacuum (Edelstein et al., 2002) such that vibrations of the GC cannot interfere with other components of the MR scanner and/or the patient. Moreover, early numerical studies were used to identify and interrupt significant transmission pathways for vibrations (Edelstein et al., 2002).

3.2.8. Vibration of connector cables—All parts attached to the GC cylinder as well as the magnet need to be able to withstand the GC vibrations and need to be designed accordingly. Mechanical vibration of the coil and cables causes mechanical fatigue of all components involved, and also leads to acoustic noise and image artefacts.

The cables connecting the GPA with the GC are particularly vulnerable. These cables are not only attached to the heavily vibrating GC, they also produce Lorentz forces themselves, since these cables carry the same high currents that are flowing in the GC, but often pass through inhomogeneous field zones leading up to the GC. One saving grace with respect to gradient cables is the fact that the same amount of current needs to flow in opposite directions on the cables leading in and out. Arranging the two cable strands to be mounted tightly together, possibly as a twisted pair or quad or coaxial arrangement, such that Lorentz forces balance themselves continuously, is the best way to handle this challenge. Twisted pair or quad arrangements are typically enclosed in a braided shield and a tear-resistant jacket. The cable shield minimizes the gradient induced interference in the RF chain. Cable vibration can also be analyzed in simulation and future fully-featured multiphysics models will include realistic cable models.

3.3. Acoustic noise

The vibrations observed in MR systems as described above are not only cause for great concern by themselves but also lead to extremely loud scanner operation, requiring hearing protection for both the patient and MR technologists (Hedeen and Edelstein, 1997). The vibrating gradient conductors cause a vibration of the GC, as well as the magnet cryostat as a whole and the inner bore wall of the MR scanner. All of these vibrations induce a pressure variation of the air particles inside and outside the bore. The cylindrically shaped bore acts as an acoustic waveguide and thus the vibration at the bore walls causes the formation of an acoustic wave in the bore (similarly to the acoustic wave propagation found in an organ pipe, by analogy). This acoustic wave can also resonate at certain frequencies, similarly to the aforementioned mechanical resonances, resulting in strongly increased sound pressure levels (SPL) at these specific acoustic resonance frequencies.

Conventional clinical MRI systems are commonly designed to stay below 100 dB. However, maximum noise levels exceeding 120 dB can occur for certain pulse sequences that excite some of the aforementioned acoustic resonances. At UHF, these SPLs are expected to increase further due to the higher vibration amplitudes responsible for acoustic wave generation. These very high SPL values represent a safety hazard for human subjects, and additional steps must be taken to reduce acoustic levels. Regulatory guidelines state that 99 dBA may not be exceeded without the use of hearing protection. One needs to be aware that the attenuation of conventional hearing protection is ~35 dB at best due to skull bone conduction.

3.3.1. Accurate analysis of acoustic sound pressure levels at UHF—Since vibrations are the sole source of significant sound generation in the MR scanner, the modeling efforts described above are directly applicable to the accurate analysis of acoustic SPLs as well. In addition, these models can incorporate fully-coupled vibroacoustic simulations, in which the effects of coupling between acoustics and vibrations are included. The significance of such a multiphysics vibroacoustic model is that highly realistic scenarios can be analyzed, describing the influences of structures in the scanner that are not captured by the cruder stand-alone analyses seen for GC in prior literature.

The Lorentz damping effect described above also has direct relevance to the prediction of acoustic levels at UHF. According to simple theory, the rule-of-thumb linear scaling of the Lorentz force with main field strength shown by Eq. (1) predicts an increase in SPL by 22.4 dB at 11.7 T compared to 1.5 T. This has led to a concern that UHF systems might produce acoustic noise levels that exceed the 140 dB peak limit (an internationally accepted legal limit for any technical equipment). In practice, however, it has been found that noise levels on whole-body UHF systems are not significantly higher than for clinical systems (Schmitt, F., Personal Communication). The aforementioned modeling efforts have shown that Lorentz damping, which results from the additional motional damping caused by the static magnetic field B_0, is likely responsible for this observation, and suggests that acoustic levels do not in fact increase linearly with main field strength (Winkler et al., 2015).

3.2.2. Reduction of acoustic SPLs—The same methods for reducing mechanical vibration outlined above will directly lead to reduced acoustic SPLs. Additionally, the acoustic waves can be influenced directly by using appropriate acoustic damping methods. However, the number of acoustic resonances is much higher as compared to the number of mechanical resonances and it is therefore much more difficult to directly avoid acoustic resonances and instead the average spectral SPL is decreased with appropriate damping techniques.

The most common present-day method for acoustic attenuation involves the use of acoustic barrier materials, which offer SPL reductions on the order of 10–30 dB. Without an intervening layer, acoustic noise would be directly transmitted from the GC to the patient bore. This means that the mechanical characteristics of the innermost cylindrical barrier surrounding the volunteer are crucial for creating an acoustically acceptable system. This inner layer commonly contains acoustic barrier material behind a rigid bore tube. In addition, special care needs to be taken at all mechanical interfaces to block the transmission of structure borne noise from the GC to the remainder of the MRI system (Mechefske, 2005).

Additional methods for acoustic noise reduction include active acoustic noise cancellation, active-passive shielding, improved Lorentz force balancing, perforated panel absorbers, and horn end pieces (Mansfield et al., 1995; Mansfield and Haywood, 2000; Mansfield et al., 2001; Mechefske et al., 2002; Chapman et al., 2003; Edelstein et al., 2005; Mechefske, 2005; Haywood et al., 2007; Li and Mechefske, 2010; Kannan et al., 2011; Li et al., 2011; Winkler et al., 2014).

3.4. Peripheral nerve stimulation (PNS)

As gradient coil and amplifier hardware performance has increased dramatically over the past few decades, one performance limit has remained constant: that being the physiological limit defined by peripheral nerve stimulation (PNS). The more rapid switching of the stronger gradients used for UHF high-resolution imaging results in high amplitude time-varying magnetic fields over a large area of the body. This gives rise to electric fields inside the human body that can depolarize nerves, with PNS usually occurring first. At first onset, this is detected as mild vibration or tingling sensations, while at higher amplitudes PNS becomes painful. Low level PNS is considered safe, but uncomfortable levels should be avoided. This results in the operation of high performance body gradients significantly below their hardware limits for sequences that require large amplitudes and/or switching rates (Budinger et al., 1991; Mansfield and Harvey, 1993; Irnich and Schmitt, 1995; Nyenhuis et al., 1997; Chronik and Rutt, 2001a; Chronik and Rutt, 2001b). In theory, as these electric field amplitudes or switching rates increase, there is a risk of cardiac stimulation, although this has never been observed in human subjects. Assuming that pulse sequences abide by regulatory guidelines for PNS, UHF systems will operate far below cardiac stimulation thresholds, now and in the future.

PNS severely limits the operation of modern-day whole body gradient systems to levels well below their hardware-limited gradient strengths and slew rates. The primary determinant of PNS thresholds is gradient coil physical size and linear region length (Zhang et al., 2003);

for larger GCs with longer linear region length, a larger area of the body is exposed to these rapidly switching fields, thereby inducing higher electric fields and higher stimulating currents. PNS thresholds can be increased by decreasing linear region length, GC size, or both, and as a result several dedicated gradient concepts have been developed to overcome these PNS limitations and to best use the gradient fields available. In particular, the concept of smaller-sized insertable GCs design for human head imaging has become attractive. These dedicated solutions will be discussed in more detail below.

4. UHF-specific gradient technology challenges: image quality

As discussed in detail above, UHF systems offer higher intrinsic SNR and therefore improved image quality. While the same gradient systems may be used at UHF as at lower fields, subtle flaws or limitations of the gradient system can become more apparent at UHF since artefacts may rise above image noise levels. The quality and reliability of the spatially and temporally varying magnetic fields are critical to high image quality in MRI. Although many sources of degradation are field strength independent, some are dependent on B_0 and can therefore become dominant sources of image quality loss at UHF.

4.1. Gradient-induced eddy currents

Besides the most obvious parameters of maximum gradient strength (G_{max}) and maximum slew rate (S_{max}), one of the most important characteristics of a GC is its level of magnetic shielding. While a strong gradient field inside the GC bore is desired for imaging, the field outside the bore, referred to as the gradient stray field, must be kept to a minimum. Gradient stray fields that impinge on conducting structures, such as those inside the magnet cryostat, induce eddy currents in these structures that produce time-varying residual fields back in the imaging volume. These fields can adversely affect image quality and need to be minimized, in particular when considering the ongoing drive toward higher performance (stronger, faster) gradients.

These residual fields scale with the amplitude of the gradient pulse that originally gave rise to them, with amplitudes up to several percent of the original pulse amplitude. To the extent that these fields can be measured and modelled as exponentially decaying B_0 and linear gradient fields, with time constants ranging from microseconds to several seconds depending on the conducting structure that gives rise to them, they can be corrected either by applying gradient “pre-emphasis” (to compensate for linear terms) or a time-varying receiver demodulation frequency (to compensate for B_0 terms). Gradient pre-emphasis consists of additional current waveform shaping applied to each of the gradient axes, designed to maximally compensate for the eddy current induced residual fields, ideally leading to correction of waveform fidelity to better than 0.1% error.

Some portion of the eddy current induced residual fields cannot be modelled as B_0 or linear magnetic field variations, and it is not possible to correct these “higher-order” fields using only the 1st order variation of the gradients themselves. Correction of these distortions is typically accomplished by warping image volumes as a post-processing step (Doran et al., 2005).

4.2. Vibrational eddy currents

In addition to the currents produced by the pulsed gradient stray field, movement of conductive parts within the magnetic field also produces eddy currents whose Lorentz forces counteract the original movement (Lenz's law). At higher static magnetic fields, these vibration-induced eddy currents will become larger and so will the associated residual fields. There are various sources of such vibrations, ranging from random building vibrations that show no time correlation to MR gradient pulsing, to GC movements that are directly correlated to the gradient pulsing.

An example of an oscillatory effect is the oscillation of the B_0 field arising from eddy currents on vibrating structures such as the thin thermal shields inside the cryostat. The amplitude of the shift in the B_0 field can be several 10's of Hz, and is exacerbated when the frequency of gradient pulsing matches the mechanical resonant frequency of the structure responsible (Wu et al., 2000). This effect can be very detrimental to spectroscopic data quality (Serrai et al., 2002) as well as to other experiments that are sensitive to B_0-homogeneity.

Larger vibration amplitudes of the GC are typical at UHF as elaborated above. These vibrations cause changes to the impedance of the GC itself due to conductor motion within a static magnetic field. Fig. 5 shows resistance vs frequency for the same whole-body GC mounted in a 3 T magnet (blue) vs 7 T magnet (red). This plots shows clear evidence of GC impedance changes that occur at certain discrete frequencies that correspond to resonant modes, i.e. the eigenmodes mentioned above. At UHF, these frequency-dependent impedance variations increase and may make it difficult for the GPA to accurately drive the GC free of distortion, and as a result, imaging artefacts may increase significantly.

As a consequence of all types of dynamic eddy current induced fields, the timings and shapes of gradient pulses become distorted and therefore all forms of encoding (spatial, spectral, diffusion) are impaired. This may lead to image blurring and ghosting in the images. For EPI, the workhorse of fMRI and diffusion based MRI, strong ghost intensities may be observed when the GC is driven at a mechanical resonance frequency, and this source of artefact becomes much more serious at UHF.

Any method that reduces the vibration amplitudes of the GC itself or at least reduces the spread of these vibrations to other components, will help to improve image quality. Additionally, introducing oscillatory eddy current compensation may help, for example reducing $N/2$ ghosting in EPI.

5. Dedicated gradient concepts suitable for UHF

Increased gradient performanceis critical for extracting the maximum benefits of UHF, as stated earlier. One explanation for this is the fact that T2 and T2* relaxation times decrease substantially at UHF, making it important to acquire image data at shorter echo times than typical of lower field strengths – this naturally puts increased demands on the gradient system. Several recent concepts implemented in an effort to achieve substantial gains in gradient performance are summarized below.

5.1. Whole body gradient coils

Modern-day clinical whole body gradient systems provide maximum gradient strengths of 80 mT/m and maximum slew rates of 200 T/m/s. While these values are impressively high, it is increasingly recognized that gradient performance will need a further boost if we are to harvest to maximum value from UHF. Recently, the Human Connectome Project has funded the development of very high performance gradient systems. Two versions have been realized: Version 1 provides a maximum gradient strength of G_{max} 100 mT/m at a maximum slew rate S_{max} of 200 T/m/s(Kimmlingen et al., 2012; Setsompop et al., 2013; Ugurbil et al., 2013), whereas version 2 provides G_{max} 300mT/m at S_{max} 200 T/m/s(Kimmlingen et al., 2012; Setsompop et al., 2013; Ugurbil et al., 2013). Version 1 uses the gradient coil that was part of the Siemens MAGNETOM 7 T system, incorporating it into a 3 T MAGNETOM Skyra magnet. In order to generate a maximum gradient strength of 100 mT/m, the GPA was updated to deliver 900 A/2250 V. Version 2 is based on a new design comprising a doubling of the number of wire layers for each gradient axis (and consequently a quadrupling of the inductance). Because of this increased inductance, four parallel GPAs are used to drive each gradient axis, to achieve the required high slew rate of 200 T/m/s. It is anticipated that "Connectome-level" gradient strengths in the range of 100–300 mT/m, quite likely with slew rates even higher than 200 T/ m/s, will be necessary before we will see fully optimized UHF image quality, particularly for diffusion imaging, but also for other SNR-demanding applications.

5.2. Head gradient coils

In order to achieve even higher spatial, spectral, and diffusion resolutions, higher gradient strengths and slew rates than those offfered by Connectome-level body-sized gradients are required. However, PNS thresholds are already severely limiting the *useable* gradient performance for whole-body coils due to the larger area of tissue exposed to the rapidly switching fields, and only modest gains are expected in the future. It is especially for this reason that high-performance human-head-sized insertable GCs have been proposed (Chronik and Rutt, 1998; Chronik et al., 2000; Tomasi et al., 2002; Wong, 2012; Handler et al., 2014; Tang et al., 2016). A number of these designs are suitable for UHF but may not have the thermal and electrical performance to tolerate the high duty cycles, currents and slew rates required for high-quality UHF imaging. Recent developments have demonstrated rapidly deployable and smaller-sized GC inserts capable of maximum gradient strengths well above 100 mT/m, and maximum slew rates in excess of 1000 T/m/s (Wade et al., 2014; Wade et al., 2016). Ultimately, it is anticipated that insertable gradients will enable the use of UHF MRI for ultra high resolution imaging of the brain and extremities without requiring any other significant hardware changes to the system. The design of insertable gradients raises significant technological challenges in addition to those encountered for more conventional systems, some of which are briefly outlined in the sections below.

5.2.1. Insertable head gradient coil construction—An insertable head gradient is a smaller-sized GC in the form of a cylindrical shell that can be inserted into a standard scanner patient bore. The inner dimensions of this type of GC need to accommodate RF head transmit and receive coils, while still leaving adequate room for the human head. One of today's most commonly used head gradient designs has an outer diameter of 670 mm

(allowing the head gradient to fit into a 680 mm warm bore magnet, which also is a good choice for a “head-only” UHF system). The inner diameter of this head gradient is ~40 cm with a linearity region diameter of about 22 cm, making it suitable for brain imaging. Fig. 6 illustrates a smaller and more easily insertable head gradient coil concept (Wade et al., 2014; Wade et al., 2016) which achieves even higher performance, showing the location of the linearity region within the GC boundaries as well as the approximate location of the insertableGCin relation to a standard scanner patient bore. The length of this coil is 330 mm dedicated to the housing of wire paths, with an additional 120 mm of length extending to the rear of the coil to pot connections and cables. The linearity region diameter is 220 mm, and the gradient efficiency is 0.2 mT/m/A. Eddy-current-induced residual fields are less than 0.1% of the primary fields following compensation.

The design and construction of head GCs is technically challenging; for one reason, very large currents are applied to a small structure in very close proximity to the patient's head, thereby introducing significant safety issues that must be managed. Compared to larger sized body gradients, the GC conductors in head inserts are spaced more closely together and need to be protected against high voltage arcing by appropriate electrically insulating materials. The higher currents employed in high-resolution imaging generate a much larger amount of heat in a more confined space, and as a result, thermal design issues are critical. Head-sized GC engineering is therefore very well suited to multiphysics-simulation-guided design, in which each of these concerns can be analyzed and optimized using the aforementioned simulation methods.

5.2.2. PNS in head gradient coils—Since the electric fields responsible for PNS result from the time-varying magnetic field incident on a cross-section of the body, one way to control PNS is to shrink the field of view (diameter of linearity region) of the GC to only the volume of interest. For example, when imaging the head, body GCs still produce a high amplitude of time-varying magnetic fields over the entire torso cross-section, which causes PNS without improving imaging quality. The advantage of smaller-sized GCs with a reduced linearity region diameter is that fields are limited primarily to the head, decreasing the amplitudes of time-varying electric fields and induced currents significantly, thereby increasing PNS thresholds substantially (Wade et al., 2016; Tan et al., 2016; Weavers et al., 2016). This permits even higher *useable* gradient performance than expected from hardware specifications alone, compared to body-sized gradient coils. There may be additional (second-order) ways to increase PNS thresholds. For example, an asymmetric head gradient design was shown theoretically to produce 30% lower electric field per unit magnetic field than an equivalent symmetric gradient coil (Tomasi et al., 2002).

5.2.3. Cooling requirements in head gradient coils—The large currents in the conductors of high performance insertable head-sized GCs cause strong resistive heating that in turn heats the surrounding gradient structure. For reasons of patient safety and mechanical integrity, it is paramount to limit the temperature rise on all bore surfaces as well as throughout the gradient coil interior. Compared to whole-body gradients, this concern is increased in these smaller architectures due to their smaller size, larger gradient strengths, higher deposited power density in the GC, and closer proximity to the patient. Head

gradients recently developed by two groups use hollow copper conductors, through which cooling fluid can flow (Wade et al., 2014; Hodge et al., 2016). It has been shown that this type of construction leads to substantially higher power dissipation capabilities and therefore much higher useable gradient currents and duty cycles.

As with vibroacoustics and other topics related to UHF GC design, the ability to accurately model temperature distributions (both spatial and temporal) within GCs using realistic multiphysics simulation environments opens up a number of new directions for current and future head gradient development, as well as for more general thermal analysis of MR GCs.

5.2.4. Vibroacoustics in head gradient coils—Since the larger currents in head insertable GCs may also cause increased vibrations and acoustic sound generation, a detailed investigation and careful design is required in order to maintain patient safety, especially as their inner surfaces are located in close proximity to the patient's ears. Ongoing research has suggested that a lower than expected increase in vibration levels and SPLs are incurred (Winkler et al., 2014). This counterintuitive observation is in part a consequence of the reduced size of head inserts. As a result of the smaller geometry, many of the vibroacoustic resonant modes fall outside the 0–3 kHz pulse sequence spectrum, thereby offering a vibroacoustic footprint that is more forgiving of the increased current load.

6. Other noteworthy challenges related to UHF technology

6.1. Static magnetic fringe field and its limitations due to physiologic effects

The fringe field of the static magnetic field B_0 is the peripheral magnetic field extending outside the scanner. There is evidence that physiological effects, such as vertigo, metallic taste, and dizziness are related to the spatial fall-off (dB_0/dz) of the fringe field and to the diamagnetic force B_0*dB_0/dz (Kangarlu et al., 1999; Liu et al., 2003; Cavin et al., 2007; Glover et al., 2007; Glover and Bowtell, 2008; Groebner et al., 2011; Budinger et al., 2016).

Actively shielded magnets are built to shape the fringe field by suppressing excessive field outside the magnet; such active shielding can only be accomplished by increasing the spatial field fall-off and thereby the diamagnetic force, which increases the aforementioned physiological effects and needs to be carefully managed. Experience from the existing base of human UHF magnets gives some empirical indication of threshold values of fringe field fall-off and diamagnetic force, below which side effects are acceptable. Table 1 shows a summary of known UHF magnets, tabulating values of dB_0/dz and B_0*dB_0/dz. One specific comparison can be highlighted in this table: an actively shielded 7 T magnet with 680 mm warm bore diameter, suitable for head-only systems, demonstrates ~50% higher diamagnetic force and thus increased physiological concerns, as compared to the 900 mm warm bore passively shielded 7 T magnet (the most common UHF magnet in existence today). More generally, the data in Table 1 shows that field strength alone is not a sufficient predictor of physiological effects. Overall, while it is clear that future advances in UHF magnet technology will increase the probability of physiological sensations, it is well understood that these transient physiological effects are relatively easily avoided by moving the subject very slowly into the UHF magnet bore.

6.2. Helium boil-off

Perhaps less obvious than all of the other UHF-related challenges described above, but equally influenced by the higher static magnetic field, is an energy transmission phenomenon that produces gradient-induced helium boil-off.

Without a static magnetic field, all the conductive layers of a magnet shield incoming fields at any significant frequency. With static magnetic field present, complex nonlinear transmission phenomena begin to appear. Electrical resistance and consequently energy deposition almost always rises dramatically with increasing static magnetic field as a result of a physical phenomenon known as “magnetoresistance” (Corruccini, 1964). For superconducting magnets with superconductors immersed in a liquid helium bath, vibrational energy acting on the thermal shield (a structure located inside the cryostat near the helium vessel) is eventually dissipated into the liquid helium, causing a helium phase transition from liquid to gas. As a result, considerable amounts of helium may be evaporated by gradient activity. Losses of up to half a liter of liquid helium per minute during intense gradient activity can be observed with older UHF systems.

This type of helium boil-off can be avoided with an understanding of the mechanical characteristics of the system. Typical UHF boil-off shows a strongly resonant behavior, with the resonant frequencies that produce the highest boil-off rate stemming from mechanical resonances of the conductive layers between the GC and the helium bath (such as the thermal shields). The vibrational characteristics at the low temperatures and the high magnetic field at the thermal shields inside the magnet therefore define the helium boil-off characteristics of the MR system. Adapting sequences to avoid these worst-case frequencies is one means to reduce helium losses, albeit not a general solution. For example, choosing a sinusoidal gradient read-out scheme for EPI pulse sequences over a trapezoidal scheme has a significant effect, as the fundamental EPI sinusoidal readout frequency is typically not higher than 1 kHz, while the mechanical resonance frequencies of greatest concern typically occur around 2 kHz. Such a sinusoidal readout train therefore offers the potential for significantly reduced boil-off (Fig. 7).

As with almost all of the concerns related to UHF gradient engineering elaborated above, a detailed investigation using multi-physics simulations can yield important insights and fundamental understanding of helium boil-off (Rausch et al.,). With this 2005 understanding comes the potential for optimizing the mechanical design of the cryostat, aiming at lower (or zero) boil-off magnets, even under the conditions of high amplitude high frequency gradient pulsing. Given the scarcity of helium as a natural resource, this is an important topic in UHF magnet engineering.

7. Conclusion

In this review, we have provided an overview of gradients and shims in UHF MRI systems. We have emphasized that gradient and shim performance substantially higher than available today will be required in order to fully realize the intrinsic benefits of UHF. We outlined the principal engineering challenges associated with high performance GCs. Specific focus was given to gradient amplifier technology, vibroacoustic footprint, eddy currents, PNS, as well

as other errors and detrimental physical effects that are exacerbated at UHF. We provided a short overview of typical state-of-the-art UHF gradient systems and their implementation, and described insertable head gradient technologies, which have become an important option for UHF systems due to their inherently higher electromagnetic and PNS performance. We have described the many benefits that come from modern multiphysics simulations, and we expect that such modeling will very strongly influence the design of high performance UHF MRI systems of the future.

Acknowledgments

The authors would like to acknowledge support from the National Sciences and Engineering Research Council of Canada for Dr. Winkler, the Burroughs-Wellcome Trust for a Collaborative Research Travel grant to Dr. Winkler, and the US National Institutes of Health grant NIH P41 EB015891.

References

Pohmann R, Speck O, Scheffer K. Signal-to-noise ratio and MR tissue parameters in human brain imaging at 3, 7, and 9.4 T using current receive coil arrays. Magn Reson Med. 2016; 75(2):801–809. [PubMed: 25820458]

Van Essen DC, Ugurbil K, Auerbach E, et al. The Human Connectome Project: a data acquisition perspective. Neuroimage. 2012; 62(4):2222–2231. [PubMed: 22366334]

Van Essen DC, Smith SM, Barch DM, Behrens TE, Yacoub E, Ugurbil K, Consortium WUMH. The WU-Minn Human Connectome Project: an overview. Neuroimage. 2013; 80:62–79. [PubMed: 23684880]

Ugurbil K, Xu J, Auerbach EJ, et al. Pushing spatial and temporal resolution for functional and diffusion MRI in the Human Connectome Project. Neuroimage. 2013; 80:80–104. [PubMed: 23702417]

Vu AT, Auerbach E, Lenglet C, Moeller S, Sotiropoulos SN, Jbabdi S, Andersson J, Yacoub E, Ugurbil K. High resolution whole brain diffusion imaging at 7 T for the Human Connectome Project. Neuroimage. 2015; 122:318–331. [PubMed: 26260428]

Hodge MR, Horton W, Brown T, et al. ConnectomeDB–Sharing human brain connectivity data. Neuroimage. 2016; 124(Pt B):1102–7. [PubMed: 25934470]

Tomasi D, Shokri-Kojori E, Volkow ND. High-resolution functional connectivity density: hub locations, sensitivity, specificity, reproducibility, and reliability. Cereb Cortex. 2016; 26(7):3249–3259. [PubMed: 26223259]

Cohen-Adad JTD, Kimmlingen R, et al. Improved Q-ball imaging using a 300 mT/m human gradient. Proc Int Soc Magn Res. 2012; 20:694.

Kimmlingen REE, Dietz P, et al. Concept and realization of high strength gradients for the human connectome project. Proc Int Soc Magn Res. 2012; 20:696.

McNab JWT, Bhat H, et al. In vivo human brain measurements of axon diameter distributions in the corpus callosum using 300 mT/m maximum gradient strength. Proc Int Soc Magn Res. 2012; 20:3563.

Setsompop IBB, Cohen-Adad J, et al. Whole-brain DSI in 4 min: sparse sampling in q-space with simultaneous multi-slice acquisition. Proc Int Soc Magn Res. 2012:693.

Tisdall DMJ, Wald LL. Improving SNR in high b-value diffusion imaging using Gmax=300 mT/m human gradients, Proc. Int Soc Magn Res. 2012; 20:2738.

Wedeen VW, LL, Cohen-Adad J, et al. In vivo imaging of fiber pathways of the human brain with ultra-high gradients. Proc Int Soc Magn Res. 2012; 20:1876.

Chapman BLW. Gradients: the heart of the MRI machine. Curr Med Imag Rev. 2006; 2(1):131–138.

Pillsbury RD, Punchard WFB. A finite-element fourier expansion technique for the design of a pulsed radial gradient system for magnetic-resonance-imaging (Mri). IEEE Trans Magn. 1985; 21(6): 2273–2275.

Turner R. A target field approach to optimal coil design. J Phys D-Appl Phys. 1986; 19(8):L147–L151.

Turner R. Minimum inductance coils. J Phys E-Sci Instrum. 1988; 21(10):948–952.

Turner R. Gradient coil design - a review of methods. Magn Reson Imag. 1993; 11(7):903–920.

Crozier S, Forbes LK, Doddrell DM. The design of transverse gradient coils of restricted length by simulated annealing. J Magn Reson Ser A. 1994; 107(1):126–128.

Mueller OMRP, Park JN, Souza SP. A general purpose non-resonant gradient power system. Proc Soc Magn Reson Med. 1991; 10:130.

Ideler KHNS, Borth G, Hagen U, Hausmann R, Schmitt F. A resonant multi purpose gradient power switch for high performance imaging. Proc Soc Magn Reson Med. 1992; 11:4044.

Mueller, OM., Park, JN., Roemer, PB., Souza, SP. A High-Efficiency 4-Switch Gto Speed-up Inverter for the Generation of Fast-Changing Mri Gradient Fields. Apec 93: Eighth Annual Applied Power Electronics Conference and Exposition; 1993. p. 806-812.

Koch KM, Rothman DL, de Graaf RA. Optimization of static magnetic field homogeneity in the human and animal brain in vivo. Prog Nucl Magn Reson Spectrosc. 2009; 54(2):69–96. [PubMed: 20126515]

Chen, CN., Hoult, DJ. Biomedical Magnetic Resonance Technology. Hilger, A., editor. New York: 2005.

Hetherington HP, Chu WJ, Gonen O, Pan JW. Robust fully automated shimming of the human brain for high-field H-1 spectroscopic imaging. Magn Reson Med. 2006; 56(1):26–33. [PubMed: 16767750]

Gruetter R, Boesch C. Fast, noniterative shimming of spatially localized signals -invivo analysis of the magnetic-field along axes. J Magn Reson. 1992; 96(2):323–334.

Gruetter R. Automatic, localized invivo adjustment of all 1st-order and 2nd-Order shim coils. Magn Reson Med. 1993; 29(6):804–811. [PubMed: 8350724]

Shen J, Rothman DL, Hetherington HP, Pan JW. Linear projection method for automatic slice shimming. Magn Reson Med. 1999; 42(6):1082–1088. [PubMed: 10571929]

Spielman DM, Adalsteinsson E, Lim KO. Quantitative assessment of improved homogeneity using higher-order shims for spectroscopic imaging of the brain. Magn Reson Med. 1998; 40(3):376–382. [PubMed: 9727940]

Pan JW, Lo KM, Hetherington HP. Role of very high order and degree B0 shimming for spectroscopic imaging of the human brain at 7 T. Magn Reson Med. 2012; 68(4):1007–1017. [PubMed: 22213108]

Juchem C, Green D, de Graaf RA. Multi-coil magnetic field modeling. J Magn Reson. 2013; 236:95–104. [PubMed: 24095841]

Juchem C, Nixon TW, McIntyre S, Boer VO, Rothman DL, de Graaf RA. Dynamic multi-coil shimming of the human brain at 7 T. J Magn Reson. 2011; 212(2):280–288. [PubMed: 21824794]

Truong TK, Darnell D, Song AW. Integrated RF/shim coil array for parallel reception and localized B-0 shimming in the human brain. Neuroimage. 2014; 103:235–240. [PubMed: 25270602]

Han H, Song AW, Truong TK. Integrated parallel reception, excitation, and shimming (iPRES). Magn Reson Med. 2013; 70(1):241–247. [PubMed: 23629974]

Stockmann JP, Witzel T, Keil B, Polimeni JR, Mareyam A, LaPierre C, Setsompop K, Wald LL. A 32-channel combined RF and B-0 shim array for 3T brain imaging. Magn Reson Med. 2016; 75(1):441–451. [PubMed: 25689977]

Winkler SASJ, Warr PA, Keil B, Watkins R, Wald LL, Rutt BK. Comparison of new element designs for combined RF-Shim arrays at 7 T. Proc Int Soc Magn Res. 2015; 23:1454.

Stockmann JWT, Blau JN, Polimeni JR, Zhao W, Keil K, Wald LL. Combined shim-RF array for highly effcient shimming of the brain at 7 T. Proc Int Soc Magn Res. 2013; 21:0665.

Mansfield P, Chapman B. Active magnetic screening of gradient coils in nmr imaging. J Magn Reson. 1986; 66(3):573–576.

Tomasi DG, Ernst T. Echo planar imaging at 4 T with minimum acoustic noise. J Magn Reson Imag. 2003; 18(1):128–130.

Oesterle C, Hennel F, Hennig J. Quiet imaging with interleaved spiral read-out. Magn Reson Imag. 2001; 19(10):1333–1337.

Edelstein WA, Hedeen RA, Mallozzi RP, El-Hamamsy SA, Ackermann RA, Havens TJ. Making MRI quieter. Magn Reson Imag. 2002; 20(2):155–163.

Taracila V, Edelstein WA, Kidane TK, Eagan TP, Baig TN, Brown RW. Analytical calculation of cylindrical shell modes: Implications for MRI acoustic noise. Concepts Magn Reson B-Magn Reson Eng. 2005; 25b(1):60–64.

Shao W, Mechefske CK. Analysis of the sound field in finite length finite in baffled cylindrical ducts with vibrating walls of finite impedance. J Acoust Society of Am. 2005; 117(4):1728–1736.

Zorumski WE. Generalized radiation impedances and reflection coefficients of circular and annular ducts. J Acoust Soc Am. 1973; 54(6):1667–1673.

Mechefske CK, Wang FL. Theoretical, numerical, and experimental modal analysis of a single-winding gradient coil insert cylinder. Magn Reson Mater Phys Biol Med. 2006; 19(3):152–166.

Mechefske CK, Geris R, Gati JS, Rutt BK. Acoustic noise reduction in a 4 T MRI scanner. Magn Reson Mater Phys Biol Med. 2002; 13(3):172–176.

Mechefske CK, Yao G, Li W, Gazdzinski C, Rutt BK. Modal analysis and acoustic noise characterization of a 4 T MRI gradient coil insert. Concepts Magn Reson B-Magn Reson Eng. 2004; 22b(1):37–49.

Winkler SAAA, Wade TP, McKenzie CA, Rutt BK. Lorentz damping and the field dependence of gradient coil vibroacoustics. Proc Int Soc Magn Res. 2015; 23:1020.

Winkler SAAA, Wade TP, McKenzie CA, Rutt BK. A traveling-wave approach to acoustic noise reduction in MR gradient coils. Proc Int Soc Magn Res. 2014; 22:4852.

Yao GZ, Mechefske CK, Rutt BK. Characterization of vibration and acoustic noise in a gradient-coil insert. Magn Reson Mater Phys Biol Med. 2004; 17(1):12–27.

Wang Y, Liu F, Crozier S. Simulation study of noise reduction methods for a split MRI system using a finite element method. Med Phys. 2015; 42(12):7122–7131. [PubMed: 26632066]

Rausch M, Gebhardt M, Kaltenbacher M, Landes H. Computer-aided design of clinical magnetic resonance imaging scanners by coupled magnetomechanical-acoustic modeling. iEEE Trans Magn. 2005; 41(1):72–81.

Lerch, R., Kaltenbacher, M., Landes, H., Hofer, M., Hoffelner, J., Rausch, M., Schinnerl, M. Advanced computer modeling of magnetomechanical transducers and their sound fields. IEEE Ultrasonics Symposium Proceedings; 2000. p. 747-758.

Liu LM, Sanchez-Lopez H, Liu F, Crozier S. Flanged-edge transverse gradient coil design for a hybrid LINAC-MRI system. J Magn Reson. 2013; 226:70–78. [PubMed: 23220182]

Liu, LM., Sanchez-Lopez, H., Poole, M., Liu, F., Crozier, S. Simulation and analysis of split gradient coil performance in MRI. 2011 Annual International Conference of the IEEE Engineering in Medicine and Biology Society (Embc); 2011. p. 4149-4152.

Jiang LZ, Havens TJ. Environmental vibration induced magnetic field disturbance in MRI magnet. IEEE Trans Appl Supercond. 2012; 22(3)

Goora FG, Han H, Ouellette M, Colpitts BG, Balcom BJ. Investigation of magnetic field gradient waveforms in the presence of a metallic vessel in magnetic resonance imaging through simulation. IEEE Trans Magn. 2013; 49(6):2920–2932.

Winkler SAAA, Wade TP, McKenzie CA, Rutt BK. Accurate vibroacoustic simulations in high performance gradient coils. Proc Int Soc Magn Res. 2014; 22:3089.

Moelker A, Wielopolski PA, Pattynama PMT. Relationship between magnetic field strength and magnetic-resonance-related acoustic noise levels. Magn Reson Mater Phys Biol Med. 2003; 16(1): 52–55.

Winkler SAAA, Wade TP, McKenzie CA, Rutt BK. Vibroacoustic noise reduction in high performance head gradient coils using ceramic inserts. Proc Int Soc Magn Res. 2016; 24:3554.

Hedeen RA, Edelstein WA. Characterization and prediction of gradient acoustic noise in MR imagers. Magn Reson Med. 1997; 37(1):7–10. [PubMed: 8978626]

Schmitt, F. Personal Communication.

Mechefske, CK. Acoustic noise reduction liner for a 4 T MRI scanner. Proceedings of the ASME International Design Engineering Technical Conferences and Computers and Information in Engineering Conference; 2005. p. 2569-2573.

Li GM, Mechefske CK. A comprehensive experimental study of micro-perforated panel acoustic absorbers in MRI scanners. Magn Reson Mater Phys Biol Med. 2010; 23(3):177–185.

Edelstein WA, Kidane TK, Taracila V, Baig TN, Eagan TP, Cheng YCN, Brown RW, Mallick JA. Active-passive gradient shielding for MRI acoustic noise reduction. Magn Reson Med. 2005; 53(5):1013–1017. [PubMed: 15844137]

Haywood B, Chapman B, Mansfield P. Model gradient coil employing active acoustic control for MRI. Magn Reson Mater Phys Biol Med. 2007; 20(5–6):223–231.

Mansfield P, Chapman BLW, Bowtell R, Glover P, Coxon R, Harvey PR. Active acoustic screening - reduction of noise in gradient coils by Lorentz force balancing. Magn Reson Med. 1995; 33(2): 276–281. [PubMed: 7707921]

Chapman BLW, Haywood B, Mansfield P. Optimized gradient pulse for use with EPI employing active acoustic control. Magn Reson Med. 2003; 50(5):931–935. [PubMed: 14587003]

Mansfield P, Haywood B. Principles of active acoustic control in gradient coil design. Magn Reson Mater Phys Biol Med. 2000; 10(2):147–151.

Mansfield P, Haywood B, Coxon R. Active acoustic control in gradient coils for MRI. Magn Reson Med. 2001; 46(4):807–818. [PubMed: 11590659]

Kannan G, Milani AA, Panahi IMS, Briggs RW. An efficient feedback active noise control algorithm based on reduced-order linear predictive modeling of FMRI acoustic noise. IEEE Trans Biomed Eng. 2011; 58(12):3303–3309. [PubMed: 21134809]

Li MF, Rudd B, Lim TC, Lee JH. In situ active control of noise in a 4 T MRI scanner. J Magn Reson Imag. 2011; 34(3):662–669.

Budinger TF, Fischer H, Hentschel D, Reinfelder HE, Schmitt F. Physiological-effects of fast oscillating magnetic-field gradients. J Comput Assist Tomogr. 1991; 15(6):909–914. [PubMed: 1939767]

Irnich W, Schmitt F. Magnetostimulation in MRI. Magn Reson Med. 1995; 33(5):619–623. [PubMed: 7596265]

Chronik BA, Rutt BK. A comparison between human magnetostimulation thresholds in whole-body and head/neck gradient coils. Magn Reson Med. 2001a; 46(2):386–394. [PubMed: 11477644]

Chronik BA, Rutt BK. Simple linear formulation for magnetostimulation specific to MRI gradient coils. Magn Reson Med. 2001b; 45(5):916–919. [PubMed: 11323819]

Mansfield P, Harvey PR. Limits to neural stimulation in echo-planar imaging. Magn Reson Med. 1993; 29(6):746–758. [PubMed: 8350717]

Nyenhuis JA, Bourland JD, Schaefer DJ. Analysis from a stimulation perspective of the field patterns of magnetic resonance imaging gradient coils. J Appl Phys. 1997; 81(8):4314–4316.

Zhang B, Yen YF, Chronik BA, McKinnon GC, Schaefer DJ, Rutt BK. Peripheral nerve stimulation properties of head and body gradient coils of various sizes. Magn Reson Med. 2003; 50(1):50–58. [PubMed: 12815678]

Doran SJ, Charles-Edwards L, Reinsberg SA, Leach MO. A complete distortion correction for MR images: I. Gradient warp correction. Phys Med Biol. 2005; 50(7):1343–1361. [PubMed: 15798328]

Wu Y, Chronik BA, Bowen C, Mechefske CK, Rutt BK. Gradient-induced acoustic and magnetic field fluctuations in a 4T whole-body MR imager. Magn Reson Med. 2000; 44(4):532–536. [PubMed: 11025508]

Serrai H, Clayton DB, Senhadji L, Zuo C, Lenkinski RE. Localized proton spectroscopy without water suppression: removal of gradient induced frequency modulations by modulus signal selection. J Magn Reson. 2002; 154(1):53–59. [PubMed: 11820826]

Setsompop K, Kimmlingen R, Eberlein E, et al. Pushing the limits of in vivo diffusion MRI for the Human Connectome Project. Neuroimage. 2013; 80:220–233. [PubMed: 23707579]

Handler WB, Harris CT, Scholl TJ, Parker DL, Goodrich KC, Dalrymple B, Van Sass F, Chronik BA. New head gradient coil design and construction techniques. J Magn Reson Imag. 2014; 39(5): 1088–1095.

Wong EC. Local head gradient coils: window(s) of opportunity. Neuroimage. 2012; 62(2):660–664. [PubMed: 22245342]

Chronik BA, Alejski A, Rutt BK. Design and fabrication of a three-axis edge ROU head and neck gradient coil. Magn Reson Med. 2000; 44(6):955–963. [PubMed: 11108634]

Chronik BA, Rutt BK. Constrained length minimum inductance gradient coil design. Magn Reson Med. 1998; 39(2):270–278. [PubMed: 9469710]

Tomasi D, Xavier RF, Foerster B, Panepucci H, Tannus A, Vidoto EL. Asymmetrical gradient coil for head imaging. Magn Reson Med. 2002; 48(4):707–714. [PubMed: 12353289]

Tang F, Liu F, Freschi F, Li Y, Repetto M, Wang Y, Crozier S. An improved asymmetric gradient coil design for high-resolution MRI head imaging. J Magn Reson. 2016 In Press.

Wade TP, Alejski A, Bartha J, Tsarapkina D, Hinks RS, McKinnon GC, Rutt BK, McKenzie CA. Design, construction and initial evaluation of a folded insertable head gradient coil. Proc Int Soc Magn Res. 2014; 23:4851.

Wade TPAA, McKenzie CA, Rutt BK. Peripheral nerve stimulation thresholds of a high performance insertable head gradient coil. Proc Int Soc Magn Res. 2016; 24:3552.

Tan ET, Lee SK, Weavers PT, Graziani D, Piel JE, Shu Y, Huston J 3rd, Bernstein MA, Foo TK. High slew-rate head-only gradient for improving distortion in echo planar imaging: Preliminary experience. J Magn Reson Imaging. 2016

Weavers PT, Shu Y, Tao S, et al. Technical Note: Compact 3 T magnetic resonance imager with high-performance gradients passes ACR image quality and acoustic noise tests. Med Phys. 2016; 43(3): 1259–1264. [PubMed: 26936710]

Groebner J, Umathum R, Bock M, Krafft AJ, Semmler W, Rauschenberg J. MR safety: simultaneous B0, dPhi/dt, and dB/dt measurements on MR-workers up to 7 T. MAGMA. 2011; 24(6):315–322. [PubMed: 21755466]

Glover PM, Bowtell R. Measurement of electric fields induced in a human subject due to natural movements in static magnetic fields or exposure to alternating magnetic field gradients. Phys Med Biol. 2008; 53(2):361–373. [PubMed: 18184992]

Cavin ID, Glover PM, Bowtell RW, Gowland PA. Thresholds for perceiving metallic taste at high magnetic field. J Magn Reson Imag. 2007; 26(5):1357–1361.

Glover PM, Cavin I, Qian W, Bowtell R, Gowland PA. Magnetic-field-induced vertigo: a theoretical and experimental investigation. Bioelectromagnetics. 2007; 28(5):349–361. [PubMed: 17427890]

Kangarlu A, Burgess RE, Zhu H, Nakayama T, Hamlin RL, Abduljalil AM, Robitaille PM. Cognitive, cardiac, and physiological safety studies in ultra high field magnetic resonance imaging. Magn Reson Imag. 1999; 17(10):1407–1416.

Liu F, Zhao H, Crozier S. Calculation of electric fields induced by body and head motion in high-field MRI. J Magn Reson. 2003; 161(1):99–107. [PubMed: 12660116]

Budinger TF, Bird MD, Frydman L, et al. Toward 20 T magnetic resonance for human brain studies: opportunities for discovery and neuroscience rationale. MAGMA. 2016; 29(3):617–639. [PubMed: 27194154]

Corruccini, RJ. National Bureau of Standards. 1964. The Electrical Properties of Aluminum for Cryogenic Electromagnets. Technical Note 218

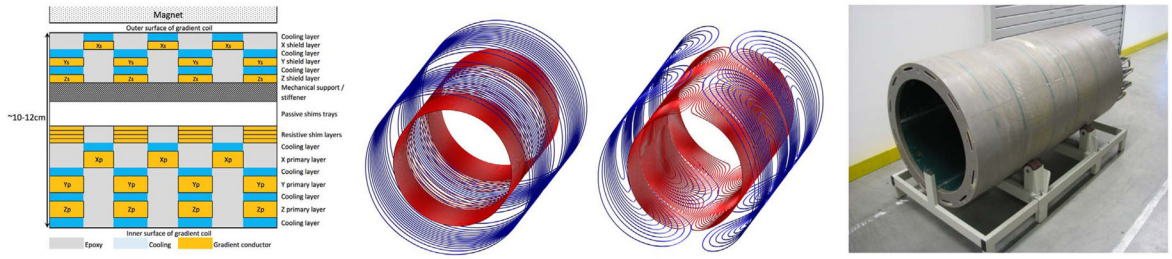

Fig. 1.

Left: Cross-section of one small portion of typical gradient coil, showing conductors, cooling layers embedded in epoxy and in relation to passive shim channel and resistive shim layers. Center left: Typical wire path for a Z gradient – inner primary / outer shield – primary wire layer in red, shield wire layer in blue. Center right: Typical wire path for a transversal gradient, i.e. X and Y gradients – primary layer in red, shield in blue. Right: Gradient coil cylinder potted in epoxy resin incorporating the gradient windings.

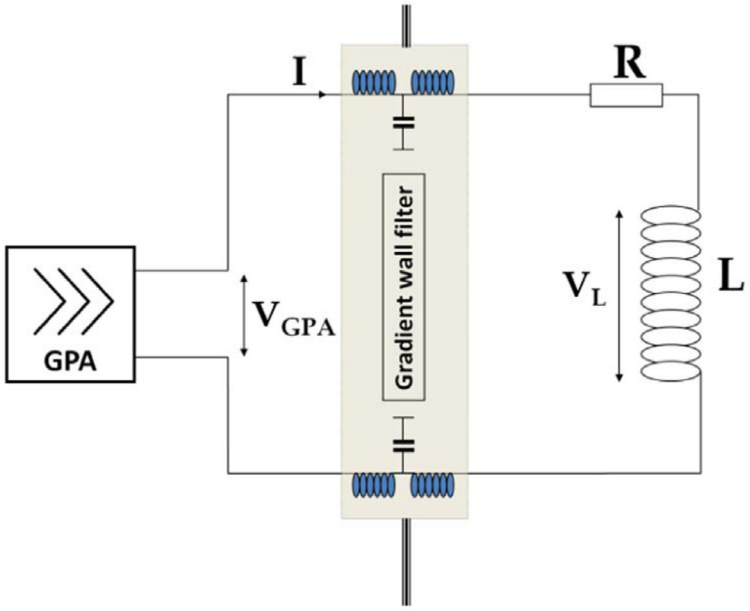

Fig. 2.
Simple / idealized circuit model of a gradient system.

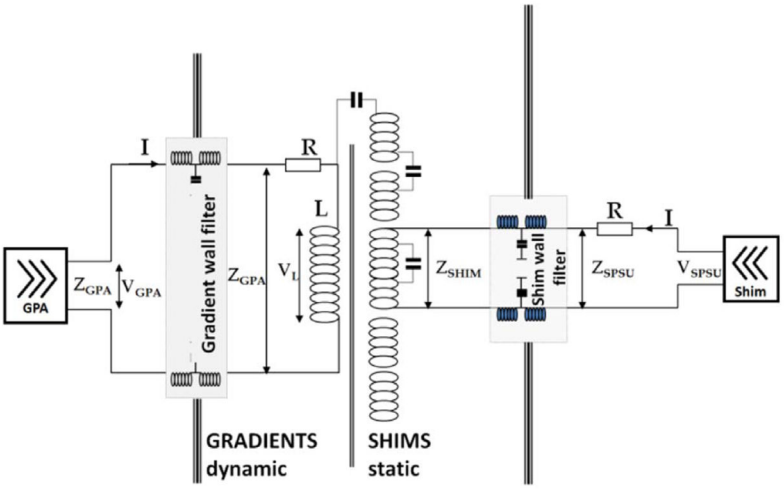

Fig. 3.

Realistic circuit model of a gradient and shim system showing coupling between gradient and shim coils.

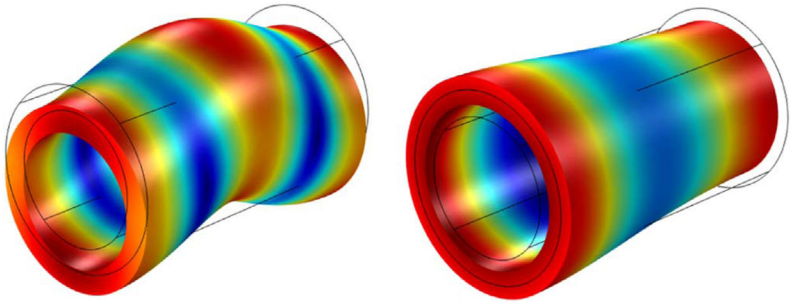

Fig. 4.

The so-called “banana” resonance mode (left) and an example of a breathing resonance mode (right) of the gradient coil cylinder. Calculation result with maximum displacements shown in red and blue, not moving parts shown in green.

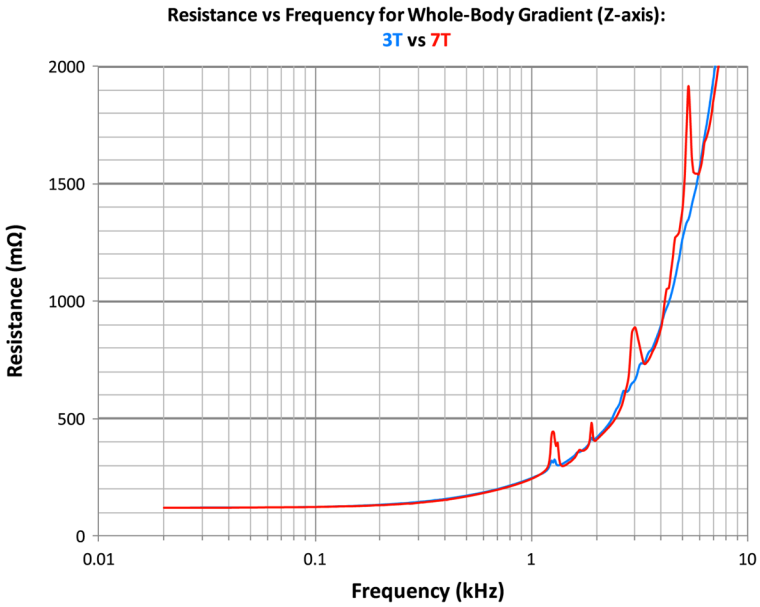

Fig. 5.

Measured resistance vs frequency dependence for 3 T and 7 T whole body gradients, showing increased amplitude of peaks corresponding to gradient mechanical resonances (eigenmodes).

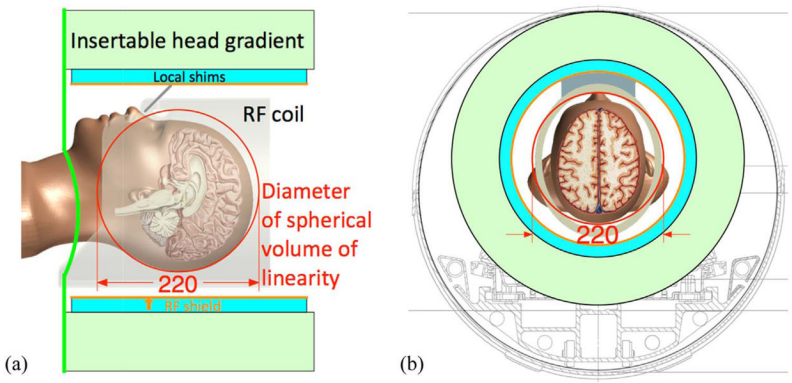

Fig. 6.

a) Insertable head gradient, including gradient / local shims / RF coil, and showing 95th%-ile male head/brain located within 220 mm diameter spherical volume of gradient linearity; b) insert gradient shown in bore of whole-body scanner, positioned on top of patient table bridge.

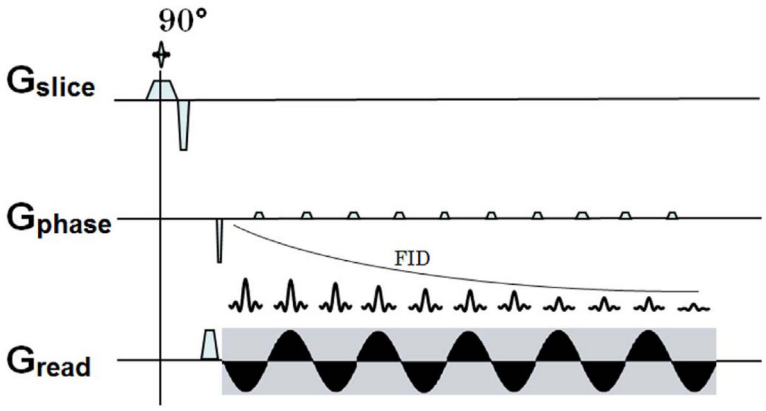

Fig. 7.

EPI pulse sequence using sinusoidal read-out gradient to avoid excitation of mechanical resonances in the cryostat.

Table 1

Fringe field fall-off dB/dz and diamagnetic force B_0*dB_0/dz along the Z-axis at X=Y=0. Magnet nomenclature is as follows: the prefix 7 T/9.4 T/10.5 T/11.7 T refers to the field strength, the numerical code 680/820/900 refers to the inner bore diameter (in mm), and the suffix AS or PS denotes whether the magnet is actively or passively shielded, respectively.

	3TWB-AS	7T680-AS	7T820-AS	7T900-AS	7T900-PS	9.4T900-PS	10.5T880-PS	11.7T680-PS
|dB/dz|max [T/m]	4.25	9.77	8.81	7.86	6.66	8.49	8.37	11.19
|B*dB/dz|max [T^2 /m]	8.48	46.08	40.32	35.99	31.63	53.08	59.73	85.18